A High–Order Spectral Algorithm for the Numerical Simulation of Layered Media with Uniaxial Hyperbolic Materials

David P. Nicholls[a]

[a] *Department of Mathematics, Statistics, and Computer Science, University of Illinois at Chicago, Chicago, IL 60607 USA*

Abstract

Electromagnetic metamaterials are artificial media assembled from components which have dimensions much smaller than the wavelength of the illuminating radiation. It has been demonstrated that these media can have properties beyond those found in conventional materials with important applications to many areas of science and engineering. Among the collection of such materials currently garnering significant attention are the Hyperbolic Metamaterials. These are highly anisotropic structures which have a hyperbolic dispersion relation due to the fact that one principal component of the relative permittivity or permeability tensor has the opposite sign of the other two. For such materials scattered wave information at all scales is transmitted far away which suggests a number of important applications, the most immediate of which is imaging objects below the diffraction limit (superlensing). Clearly it is of great current interest to have numerical simulation capabilities for these fascinating materials. As the hyperbolic response is quite strong and its nature is very sensitive, numerical simulations of these configurations should be robust and highly accurate. For this reason we focus on High–Order Spectral algorithms which efficiently produce high fidelity solutions. More specifically, we describe a High–Order Perturbation of Surfaces approach which enjoys the greatly reduced operation counts and memory savings of interfacial methods while avoiding the complexities and indefinite linear systems faced by Integral Equation algorithms. We give a full discussion of our formulation in terms of Impedance–Impedance Operators

Email address: davidn@uic.edu (David P. Nicholls)

(which avoids spurious singularities of other formulations) and implementation details, followed by numerical validation and simulation of results which appear in the engineering literature.

Keywords: High–Order Spectral Methods, Layered Media, Uniaxial Hyperbolic Materials, Linear Wave Scattering, High–Order Perturbation of Surfaces Methods.
MSC Codes: 65N35; 65N12; 78A45; 78M22; 35Q60; 35J05.

---

1. Introduction

Electromagnetic metamaterials are artificial media assembled from components which have dimensions much smaller than the wavelength of the illuminating radiation. It has been demonstrated that these media can have properties beyond those found in conventional materials with important applications to many areas of science and engineering [1, 2, 3, 4, 5, 6, 7]. The recent wave of interest in metamaterials was ushered in by the realization of negative index materials (first envisioned by Veselago [8] in 1968) that have permittivity, ϵ, and permeability, μ, simultaneously negative. These have been demonstrated experimentally [9] and allow one to ponder the possibility of perfect cloaks, sub–wavelength imaging, and superlensing to name just a few novel applications [2]. We refer the interested reader to the following survey articles for more examples and details of how such materials are constructed [4, 5, 6, 7].

Among the collection of metamaterials currently garnering significant attention are the so–called Hyperbolic Metamaterials (HMMs). These HMMs are highly anisotropic structures which have a hyperbolic dispersion relation due to the fact that one principal component of the relative permittivity or permeability tensor has the *opposite* sign of the other two. (From here we focus on non–magnetic materials where the permeability tensor is the identity.) More specifically, if the permittivity tensor is

$$\underline{\underline{\epsilon}} = \begin{pmatrix} \epsilon_x & 0 & 0 \\ 0 & \epsilon_y & 0 \\ 0 & 0 & \epsilon_z \end{pmatrix},$$

it is not difficult to construct *uniaxial* HMMs ($\epsilon_x = \epsilon_y$) where $\mathrm{Re}\{\epsilon_x\}\,\mathrm{Re}\{\epsilon_z\} < 0$ [3]. In particular, these authors consider thin alternating layers of metal

and dielectric which feature effective permittivities

$$\epsilon_x = \frac{d_m\epsilon_m + d_d\epsilon_d}{d_m + d_d} = \frac{\epsilon_m + \eta\epsilon_d}{1+\eta},$$
$$\frac{1}{\epsilon_z} = \frac{d_m\epsilon_m^{-1} + d_d\epsilon_d^{-1}}{d_m + d_d} = \frac{1}{1+\eta}\left(\frac{1}{\epsilon_m} + \frac{\eta}{\epsilon_d}\right).$$

Here ϵ_m and ϵ_d are the permittivities of the metal and dielectric, respectively, and $\eta = d_d/d_m$ is the ratio of the layer thicknesses. With $\epsilon_d > 0$ and $\mathrm{Re}\{\epsilon_m\} < 0$ it is easy to see how an HMM could be built.

To explain the possibilities of these HMMs we recall that, in a homogeneous material layer, a plane–wave solution, $\exp(i\alpha x + i\gamma z)$, of the time–harmonic Maxwell equations in Transverse Magnetic (TM) polarization will satisfy the dispersion relation

$$\frac{\alpha^2}{\epsilon_z} + \frac{\gamma^2}{\epsilon_x} = k_0^2,$$

where $k_0 = \omega/c_0$, ω is the frequency of the radiation, and c_0 is the speed of light in the vacuum. In a natural dielectric $\epsilon_x, \epsilon_z > 0$ and the wavevectors (α, γ) form an ellipse. Of fundamental importance, if α is small then γ is real and the solution is propagating, while if α is large then γ is complex with $\mathrm{Im}\{\gamma\} \geq 0$. Such solutions decay exponentially and are termed evanescent. Only long wavelengths propagate information away from the material and information at short wavelengths is lost exponentially quickly. This is the diffraction limit.

By contrast, if one can arrange $\epsilon_x\epsilon_z < 0$ then the dispersion relation delivers a *hyperbola* and for all choices of α we have γ real so that *all* wavelengths are propagating. Information at *all* scales is, in theory, transmitted far away from an HMM. This property suggests a number of important applications for these hyperbolic materials, the most immediate of these is the possibility of imaging objects *below* this diffraction limit (of a natural, elliptic, dielectric) [3]. We direct the interested reader to the surveys [4, 5, 6] which describe devices which have been built that can achieve this superlensing, despite the inevitable losses due to absorption.

Interestingly, natural Hyperbolic Materials (HMs) have been identified which display the strong anisotropy of the HMMs discussed above, most notably hexagonal Boron Nitride (hBN) [10, 11]. Though our developments do not depend upon this choice, we will focus on hBN in this contribution

as it seems a most promising candidate for subwavelength imaging and other applications. Of particular relevance are its low losses, nanoscale unit cells, and capability of demonstrating both Type I ($\epsilon_x > 0$ and $\epsilon_z < 0$) and Type II ($\epsilon_x < 0$ and $\epsilon_z > 0$) hyperbolicity [10]. (In most publications [4, 6, 11] one uses the notation $\epsilon_z = \epsilon_\parallel$ for the component parallel to the anistropy axis and $\epsilon_x = \epsilon_\perp$ for the component perpendicular, though this is not universal [5].)

Unsurprisingly, it is of great current interest to have numerical simulation capabilities for these fascinating materials. As the hyperbolic response of hBN is quite strong (the reflectivity can be enhanced by several orders of magnitude) and its nature is very sensitive (it is only seen on the range of tens of nanometers) [10], numerical simulations of these configurations should be robust and highly accurate. For this reason we focus on High–Order Spectral (HOS) algorithms [12, 13, 14] which efficiently produce high fidelity solutions.

All of the classical numerical algorithms are available for the simulation of this problem (e.g., Finite Difference Methods [15], Finite Element Methods (FEMs) [16], Discontinuous Galerkin Methods [17], Spectral Element Methods [13], and Spectral Methods [12, 14]). Of particular interest to engineers and scientists are black–box FEM solvers, most notably COMSOL Multiphysics [18], see e.g. [19, 20]. However, these volumetric approaches are greatly disadvantaged with an unnecessarily large number of unknowns for the piecewise homogeneous problems we consider here.

Surface methods are orders of magnitude faster by comparison due to the greatly reduced number of unknowns required to resolve a computation. In addition, these methods enforce far–field boundary conditions exactly, e.g., through their use of the Green function [21, 22]. As a result, these approaches are an important alternative which are becoming more widely used by engineers. Among these interfacial methods, the most important are those based upon Integral Equations (IEs) [21, 23], but these face difficulties. Most have been addressed by (i.) the use of sophisticated quadrature rules to deliver HOS accuracy; (ii.) the design of preconditioned iterative solvers with suitable acceleration [24]; and (iii) new strategies to avoid periodizing the Green function [25, 26, 27, 28, 29, 30, 31, 32]. As a result, these are an important alternative to volumetric approaches, but two properties render them non–competitive for the *parameterized* layered media problems we consider as compared with the methods we advocate here: (i.) For geometries specified by the real value ε (the departure of the interface shapes from flat), an IE

solver will return the scattering returns only for one value of ε. If this value is changed then the solver must be run again; (ii.) the dense, non–symmetric positive definite systems of linear equations which must be inverted with each simulation.

As we have shown, see e.g. [33, 34, 35, 36], a "High–Order Perturbation of Surfaces" (HOPS) approach can convincingly address these concerns. These formulations maintain the useful properties of classical IE algorithms (e.g., surface formulation and exact enforcement of far–field conditions) while avoiding the flaws listed above: (i.) Since HOPS methods are built upon expansions in the perturbation parameter, ε, once the Taylor coefficients are recovered, it is simply a matter of summing these (rather than beginning a new simulation) for any given choice of ε to recover the scattering quantities; (ii.) due to the perturbative nature of the scheme, at every Taylor order one need only invert a single, sparse operator corresponding to the order–zero (flat–interface) approximation of the problem.

Regardless of method used, the formulation of the governing equations strongly influences the performance of these approaches. With this in mind, following the guidance in [37, 38], we recently investigated the surface formulation of this problem in terms of Impedance–Impedance Operators (IIOs) [34, 39] which avoid the Dirichlet eigenvalues that plague the Dirichlet–Neumann Operators (DNOs) of more straightforward statements [40]. This non–overlapping Domain Decomposition Method (DDM) was first described for Laplace's equation by Lions [41] and adapted to the Helmholtz problem by Després [42, 43, 37]. On interior layers these IIOs are unitary and they deliver a very well–conditioned algorithm. We utilize a formulation of the problem in terms of IIOs here which we restrict to two dimensions in the current contribution.

Before leaving our discussion of numerical approaches, we mention the recent work of J. Lin [44] on IE methods for HMs. In this delicate and careful study, Lin describes a novel method for simulating the Green function associated to the relevant indefinite Helmholtz equation. This requires sophisticated grid refinement technology to resolve the boundary between regions of elliptic and hyperbolic behavior of the fundamental solution. In contrast to this IE algorithm (whose utilization of the Green function requires this refinement), the approach outlined in this work does not require such considerations provided that the exciting source is *not* contained in the HM, e.g., plane–wave incidence from above/below through a dielectric.

The rest of the paper is organized as follows: In § 2 we state the governing

equations for scattering of linear waves by a periodic layered medium with special discussions of the field equations in § 2.1, the interfacial boundary conditions in § 2.2, and transparent boundary conditions in § 2.3. We recall our DDM in § 3 and our HOPS scheme in § 4. Finally, we conclude with numerical results in § 5 featuring specific discussions of implementation in § 5.1, validation in § 5.2, and comparision with results in the literature in § 5.3.

2. Governing Equations

We begin with the constituitive relations between the electric displacement, $\mathbf{D}$, the magnetic induction, $\mathbf{B}$, the electric field, $\mathbf{E}$, and the magnetic field, $\mathbf{H}$,

$$\mathbf{D} = \epsilon_0 \underline{\underline{\epsilon}} \mathbf{E}, \quad \mathbf{B} = \mu_0 \underline{\underline{\mu}} \mathbf{H},$$

where ϵ_0 and μ_0 are the permittivity and permeability of the vacuum, and $\underline{\underline{\epsilon}}$ and $\underline{\underline{\mu}}$ are the relative permittivity and permeability tensors [45]. We focus upon non–magnetic materials so that $\underline{\underline{\mu}} = \underline{\underline{I}}$, and, after diagonalization, we have

$$\underline{\underline{\epsilon}} = \begin{pmatrix} \epsilon_x & 0 & 0 \\ 0 & \epsilon_y & 0 \\ 0 & 0 & \epsilon_z \end{pmatrix}.$$

Using these, the time–harmonic Maxwell equations (in the absence of currents and charges) become

$$\text{curl}\,[\mathbf{E}] = i\omega \mathbf{B} = i\omega\mu_0 \mathbf{H}, \tag{1a}$$

$$\text{curl}\,[\mathbf{H}] = -i\omega \mathbf{D} = -i\omega\epsilon_0 \underline{\underline{\epsilon}} \mathbf{E}, \tag{1b}$$

where time dependence of the form $\exp(-i\omega t)$ has been factored out.

2.1. Field Equation

We now seek a solution to (1) in Transverse Magnetic (TM) polarization so that all quantities are y–invariant (the transverse direction) and the magnetic field has the form $\mathbf{H} = (0, v(x,z), 0)^T$. To accomplish this we write (1) entirely in terms of $\mathbf{H}$ and, in turn, v. By solving (1b) for $\mathbf{E}$ and inserting this into (1a) we find

$$\text{curl}\left[-\frac{1}{i\omega\epsilon_0} \underline{\underline{\epsilon}}^{-1} \text{curl}\,[\mathbf{H}] \right] = i\omega\mu_0 \mathbf{H}. \tag{2}$$

Upon using the y–invariance of v we find that that the y–component of (2) becomes

$$\operatorname{div}[A\nabla v] + k_0^2 v = 0,$$

and

$$A = \begin{pmatrix} (1/\epsilon_z) & 0 \\ 0 & (1/\epsilon_x) \end{pmatrix},$$

which is *not* the inverse of $\underline{\underline{\epsilon}}$.

Remark 2.1. *We note that the same derivation could be conducted for Transverse Electric (TE) polarization resulting in the governing equation*

$$div[(1/\epsilon_y)\nabla v] + k_0^2 v = 0,$$

which, while interesting, is standard and can be treated with existing methods [46].

Remark 2.2. *In the case of an isotropic material, $\underline{\underline{\epsilon}} = \epsilon_r \underline{\underline{I}}$, we find the familiar Helmholtz equation*

$$\Delta v + \epsilon_r k_0^2 v = 0.$$

Remark 2.3. *As we mentioned above, rather than model an HMM we chose to simulate a natural HM, namely hBN. For this we used the permittivity specified in [11]*

$$\epsilon_m = \epsilon_{\infty,m}\left(1 + \frac{(\omega_{LO,m})^2 - (\omega_{TO,m})^2}{(\omega_{TO,m})^2 - \omega^2 - i\omega\Gamma_m}\right), \quad m \in \{\|, \perp\},$$

where

$$\epsilon_{\infty,\perp} = 4.87, \quad \Gamma_\perp = 5\ cm^{-1}, \quad \omega_{TO,\perp} = 1370\ cm^{-1}, \quad \omega_{LO,\perp} = 1610\ cm^{-1},$$

and

$$\epsilon_{\infty,\|} = 2.95, \quad \Gamma_\| = 4\ cm^{-1}, \quad \omega_{TO,\|} = 780\ cm^{-1}, \quad \omega_{LO,\|} = 830\ cm^{-1}.$$

From these we form

$$\underline{\underline{\epsilon}}^{hBN} = \begin{pmatrix} \epsilon_\perp & 0 & 0 \\ 0 & \epsilon_\perp & 0 \\ 0 & 0 & \epsilon_\| \end{pmatrix}. \tag{3}$$

2.2. Interfacial Boundary Conditions

At this point we fixate upon a (y–invariant) layered structure with M interfaces located at

$$z = a^{(m)} + g^{(m)}(x), \quad 1 \leq m \leq M,$$

which are d–periodic,

$$g^{(m)}(x+d) = g^{(m)}(x), \quad 1 \leq m \leq M,$$

see Figure 1. These define the $(M+1)$ domains

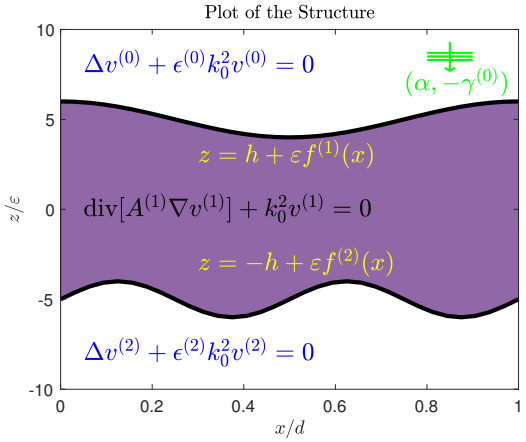

Figure 1: Plot of the structure under consideration: Graphene affixed to both the upper and lower sides of the hyperbolic material, under an isotropic dielectric ($\epsilon^{(0)}$) mounted on another isotropic dielectric ($\epsilon^{(2)}$). Structure rescaled by the period in the x coordinate and the maximum amplitude in the z coordinate.

$$S^{(0)} = \left\{(x,z) \mid z > a^{(1)} + g^{(1)}(x)\right\},$$
$$S^{(m)} = \left\{(x,z) \mid a^{(m+1)} + g^{(m+1)}(x) < z < a^{(m)} + g^{(m)}(x)\right\}, \quad 1 \leq m \leq M-1,$$
$$S^{(M)} = \left\{(x,z) \mid z < a^{(M)} + g^{(M)}(x)\right\},$$

with upward pointing normals

$$\mathbf{N}^{(m)} = \begin{pmatrix} -\partial_x g^{(m)} \\ 0 \\ 1 \end{pmatrix}.$$

These domains are filled with homogeneous non–magnetic materials with relative permittivity tensors $\underline{\underline{\epsilon}}^{(m)}$, and the uppermost and lowermost layers are isotropic dielectrics so that for $m \in \{0, M\}$, $\underline{\underline{\epsilon}}^{(m)} = \epsilon^{(m)}\underline{\underline{I}}$, $\epsilon^{(m)} \in \mathbf{R}^+$. Additionally, we consider the case where two–dimensional materials are present at the layer interfaces which we model with an interfacial current [47]. The structure is illuminated from above by radiation of frequency ω at angle θ that has the form

$$v^i = e^{i\alpha x - i\gamma^{(0)} z}, \quad \alpha = \sqrt{\epsilon^{(0)}} k_0 \sin(\theta), \quad \gamma^{(0)} = \sqrt{\epsilon^{(0)}} k_0 \cos(\theta).$$

The derivations in the previous section demonstrate that the transverse component of the magnetic field in layer $0 \leq m \leq M$, $v^{(m)}$, is governed by a Helmholtz equation of the form

$$\text{div}\left[A^{(m)} \nabla v^{(m)}\right] + k_0^2 v^{(m)} = 0, \quad 0 \leq m \leq M, \tag{4}$$

where

$$A^{(m)} = \begin{pmatrix} (1/\epsilon_z^{(m)}) & 0 \\ 0 & (1/\epsilon_x^{(m)}) \end{pmatrix},$$

which must be supplemented with appropriate boundary conditions. First, each of the fields is quasiperiodic

$$v^{(m)}(x + d, z) = e^{i\alpha d} v^{(m)}(x, z), \quad 0 \leq m \leq M. \tag{5}$$

Next, at the interfaces $z = a^{(m)} + g^{(m)}(x)$, we know that, in the presence of interfacial currents, the tangential components of the electric and magnetic fields must satisfy [47]

$$\mathbf{N}^{(m)} \times \mathbf{E} = 0, \quad \mathbf{N}^{(m)} \times \mathbf{H} = \left|\mathbf{N}^{(m)}\right| \mathbf{j}_s^{(m)}, \quad 1 \leq m \leq M.$$

where $\mathbf{j}_s^{(m)}$ is the surface current at the m–th interface. Following [47], and inspired by Ohm's Law, we model this with the relation

$$\mathbf{j}_s^{(m)} = \sigma^{(m)} \left(\frac{\mathbf{E}^{(m)} \cdot \mathbf{T}^{(m)}}{\mathbf{T}^{(m)} \cdot \mathbf{T}^{(m)}} \right) \mathbf{T}^{(m)}, \quad 1 \leq m \leq M,$$

where $\mathbf{T}^{(m)}$ is a tangent to the interface.

Using a straightforward generalization of [47], in TM polarization the tangential continuity of the electric field yields

$$-\mathcal{N}^{\ell}(m-1)[v^{(m-1)}] - \mathcal{N}^{u}(m)[v^{(m)}] = \nu^{(m)}, \quad 1 \leq m \leq M, \tag{6}$$

where

$$\nu^{(m)} = \begin{cases} \mathcal{N}^{\ell}(0)[v^i], & m = 1, \\ 0, & m > 1, \end{cases}$$

and the $A^{(m)}$–modified upper/lower exterior–pointing surface normal derivatives are defined by

$$\begin{aligned} \mathcal{N}^{u}(m)[v^{(m)}] &:= \mathbf{N}^{(m)} \cdot \left(A^{(m)} \nabla v^{(m)} \right), && z = a^{(m)} + g^{(m)}(x), \\ \mathcal{N}^{\ell}(m)[v^{(m)}] &:= -\mathbf{N}^{(m+1)} \cdot \left(A^{(m)} \nabla v^{(m)} \right), && z = a^{(m+1)} + g^{(m+1)}(x). \end{aligned}$$

Continuing, the tangential boundary condition on the magnetic field gives

$$v^{(m-1)} - v^{(m)} + \left| \mathbf{N}^{(m)} \right|^{-1} p^{(m)} \mathcal{N}^{u}(m)[v^{(m)}] = \xi^{(m)}, \quad 1 \leq m \leq M, \tag{7}$$

where

$$\xi^{(m)} = \begin{cases} -v^i, & m = 1, \\ 0, & m > 1. \end{cases}$$

Remark 2.4. *Arguably the most influential two–dimensional material in the field of plasmonics is graphene [48, 49]. To give a flavor of the form which $\sigma^{(m)}$ might take we note that, while the correct modeling of the electromagnetic properties of graphene is still open, one reasonable choice for the surface current is a Drude model [48, 49] of the form*

$$\hat{\sigma}_D = \frac{\sigma_D}{\epsilon_0 c_0}, \quad \sigma_D = \sigma_0 \left(\frac{4E_f/\pi}{\Gamma - i\hbar\omega} \right), \quad \sigma_0 = \pi \epsilon_0 c_0 \alpha, \tag{8}$$

where α is the fine structure constant, $E_F > 0$ is the (local) Fermi level position, and $\Gamma := \hbar\gamma$, where $\hbar$ is the reduced Planck's constant and γ is the relaxation rate. In our simulations we used $E_F = 0.45\ eV$ and $\Gamma = 2.6\ meV$.

2.3. Transparent Boundary Conditions and the Dispersion Relation

We require two more boundary conditions to specify a unique solution: The Upward and Downward Propagating Conditions (UPC/DPC). We derive the DPC and simply state the UPC, but for each we require artificial boundaries, $\{z = \overline{a}\}$ and $\{z = \underline{a}\}$, where

$$\overline{a} > a^{(1)} + \left| g^{(1)} \right|_{L^\infty}, \quad \underline{a} < a^{(M)} - \left| g^{(M)} \right|_{L^\infty}.$$

For the DPC we seek plane–wave solutions of the form

$$e^{i\alpha_p x - i\gamma_p^{(M)}(z-\underline{a})}, \quad \alpha_p = \alpha + \frac{2\pi p}{d}.$$

These are solutions of (4) in $\{z < \underline{a}\}$ if

$$\frac{1}{\epsilon_z^{(M)}}(i\alpha_p)^2 + \frac{1}{\epsilon_x^{(M)}}(i\gamma_p^{(M)})^2 + k_0^2 = 0,$$

which can be simplified to the *Dispersion Relation* for uniaxial materials in TM polarization

$$\frac{\alpha_p^2}{\epsilon_z^{(M)}} + \frac{(\gamma_p^{(M)})^2}{\epsilon_x^{(M)}} = k_0^2. \tag{9}$$

Notice that if the M–th layer is isotropic then $\epsilon_x^{(M)} = \epsilon_z^{(M)} = \epsilon^{(M)}$ and one rediscovers the classical dispersion relation,

$$\alpha_p^2 + (\gamma_p^{(M)})^2 = \epsilon^{(M)} k_0^2.$$

In order to specify the DPC we make the following choice for $\gamma_p^{(M)}$,

$$\gamma_p^{(M)} = \left(\epsilon_x^{(M)} k_0^2 + \left(\frac{-\epsilon_x^{(M)}}{\epsilon_z^{(M)}} \right) \alpha_p^2 \right)^{1/2}, \quad \mathrm{Im}\left\{ \gamma_p^{(M)} \right\} \geq 0,$$

which guarantees that solutions are bounded as $z \to -\infty$. Separation of variables gives

$$v^{(M)}(x,z) = \sum_{p=-\infty}^{\infty} \hat{\mu}_p e^{i\alpha_p x - i\gamma_p^{(M)}(z-\underline{a})},$$

and we observe that

$$v^{(M)}(x,\underline{a}) = \sum_{p=-\infty}^{\infty} \hat{\mu}_p e^{i\alpha_p x} = \mu(x), \quad \hat{\mu}_p = \frac{1}{d}\int_0^d \mu(x) e^{-i\alpha_p x}\, dx.$$

It is a simple matter to compute

$$\partial_z v^{(M)}(x,\underline{a}) = \sum_{p=-\infty}^{\infty} (-i\gamma_p^{(M)}) \hat{\mu}_p e^{i\alpha_p x} =: T^{(M)}[\mu],$$

which defines the order–one Fourier multiplier $T^{(M)}$. From these calculations it is clear that the DPC can be specified transparently at the artificial boundary with

$$\partial_z v^{(M)} - T^{(M)}[v^{(M)}] = 0, \quad z = \underline{a}. \tag{10}$$

In a similar fashion [39], the UPC can be specified by

$$\partial_z v^{(0)} + T^{(0)}[v^{(0)}] = 0, \quad z = \overline{a}, \tag{11}$$

where

$$T^{(0)}[\mu] := \sum_{p=-\infty}^{\infty} (-i\gamma_p^{(0)})\hat{\mu}_p e^{i\alpha_p x}.$$

Gathering all of our developments (Equations (4), (7), (6), (11), (10), and (5)) together we find the following set of governing equations

$$\begin{aligned}
&\operatorname{div}\left[A^{(m)}\nabla v^{(m)}\right] + k_0^2 v^{(m)} = 0, && 0 \le m \le M, && \text{(12a)}\\
&v^{(m-1)} - v^{(m)} + \left|\mathbf{N}^{(m)}\right|^{-1} p^{(m)}\mathcal{N}^u(m)[v^{(m)}] = \xi^{(m)}, && 1 \le m \le M, && \text{(12b)}\\
&-\mathcal{N}^\ell(m-1)[v^{(m-1)}] - \mathcal{N}^u(m)[v^{(m)}] = \nu^{(m)}, && 1 \le m \le M, && \text{(12c)}\\
&\partial_z v^{(0)} + T^{(0)}[v^{(0)}] = 0, && z = \overline{a}, && \text{(12d)}\\
&\partial_z v^{(M)} - T^{(M)}[v^{(M)}] = 0, && z = \underline{a}, && \text{(12e)}\\
&v^{(m)}(x+d,z) = e^{i\alpha d} v^{(m)}(x,z). && && \text{(12f)}
\end{aligned}$$

3. A Non–Overlapping Domain Decomposition

Following our previous work [39], and for completeness of presentation, we restate (12) using a Non–Overlapping Domain Decomposition. For this we follow the lead of Després [42, 43] by using carefully chosen Impedance–Impedance Operators (IIOs) which are free of the artificial singularities which plague other surface operators such as Dirichlet–Neumann Operators (DNOs). To summarize these developments we begin by defining the order–r Fourier multipliers

$$Y^{(m)}[\phi] := \sum_{p=-\infty}^{\infty} \widehat{Y^{(m)}}_p \hat{\phi}_p e^{i\alpha_p x}, \quad Z^{(m)}[\phi] := \sum_{p=-\infty}^{\infty} \widehat{Z^{(m)}}_p \hat{\phi}_p e^{i\alpha_p x},$$
$$\left|\widehat{Y^{(m)}}_p\right|, \left|\widehat{Z^{(m)}}_p\right| \sim \left(1 + |p|^2\right)^{r/2}, \quad r \in \{0, 1\},$$

and rearrange the boundary conditions, (12b) & (12c), by the operator

$$P^{(m)} = \begin{pmatrix} -Y^{(m)} & -I \\ Z^{(m)} & -I \end{pmatrix},$$

giving

$$\left\{\mathcal{N}^{\ell}(m-1)[v^{(m-1)}] - Y^{(m)}[v^{(m-1)}]\right\} + \left\{\mathcal{N}^{u}(m)[v^{(m)}] + Y^{(m)}[v^{(m)}]\right\}$$
$$-Y^{(m)}[\left|\mathbf{N}^{(m)}\right|^{-1} p^{(m)}\mathcal{N}^{u}(m)v^{(m)}] = -Y^{(m)}[\xi^{(m)}] - \nu^{(m)}, \tag{13a}$$
$$\left\{\mathcal{N}^{\ell}(m-1)[v^{(m-1)}] + Z^{(m)}[v^{(m-1)}]\right\} + \left\{\mathcal{N}^{u}(m)[v^{(m)}] - Z^{(m)}[v^{(m)}]\right\}$$
$$+Z^{(m)}[\left|\mathbf{N}^{(m)}\right|^{-1} p^{(m)}\mathcal{N}^{u}(m)v^{(m)}] = Z^{(m)}[\xi^{(m)}] - \nu^{(m)}. \tag{13b}$$

We select $(Y^{(m)}+Z^{(m)})$ invertible so that this transformation can be inverted, and point out that Després made the choice $Y^{(m)} = Z^{(m)} = i\eta$, $\eta \in \mathbf{R}^{+}$ so that $r = 0$ [42, 43].

In light of (13) it is natural to define the surface impedances

$$U^{(m),\ell}(x) := \mathcal{N}^{\ell}(m)[v^{(m)}] - Y^{(m+1)}[v^{(m)}],$$
$$U^{(m),u}(x) := \mathcal{N}^{u}(m)[v^{(m)}] - Z^{(m)}[v^{(m)}],$$
$$\tilde{U}^{(m),\ell}(x) := \mathcal{N}^{\ell}(m)[v^{(m)}] + Z^{(m+1)}[v^{(m)}],$$
$$\tilde{U}^{(m),u}(x) := \mathcal{N}^{u}(m)[v^{(m)}] + Y^{(m)}[v^{(m)}],$$

and, upon using these to solve for $\{v^{(m)}, \mathcal{N}^{u}(m)[v^{(m)}]\}$ in terms of $\{U^{(m),u}, \tilde{U}^{(m),u}\}$, we find that the boundary conditions (13) become

$$U^{(m-1),\ell} + \tilde{U}^{(m),u} + F^{(m)}U^{(m),u} + \tilde{F}^{(m)}\tilde{U}^{(m),u} = \zeta^{(m)},$$
$$\tilde{U}^{(m-1),\ell} + U^{(m),u} + G^{(m)}U^{(m),u} + \tilde{G}^{(m)}\tilde{U}^{(m),u} = \psi^{(m)},$$

where

$$\zeta^{(m)} = -\nu^{(m)} - Y^{(m)}[\xi^{(m)}],$$
$$\psi^{(m)} = -\nu^{(m)} + Z^{(m)}[\xi^{(m)}],$$
$$F^{(m)} = -Y^{(m)}\left[p^{(m)}\left|\mathbf{N}^{(m)}\right|^{-1} Y^{(m)}\right]\left(Y^{(m)} + Z^{(m)}\right)^{-1},$$
$$\tilde{F}^{(m)} = -Y^{(m)}\left[p^{(m)}\left|\mathbf{N}^{(m)}\right|^{-1} Z^{(m)}\right]\left(Y^{(m)} + Z^{(m)}\right)^{-1},$$
$$G^{(m)} = Z^{(m)}\left[p^{(m)}\left|\mathbf{N}^{(m)}\right|^{-1} Y^{(m)}\right]\left(Y^{(m)} + Z^{(m)}\right)^{-1},$$
$$\tilde{G}^{(m)} = Z^{(m)}\left[p^{(m)}\left|\mathbf{N}^{(m)}\right|^{-1} Z^{(m)}\right]\left(Y^{(m)} + Z^{(m)}\right)^{-1}.$$

We direct the interested reader to our previous work [39] for full details.

To close (and simplify) this system of equations we introduce the following Impedance–Impedance Operators (IIOs) which are a generalization of those defined in [39].

Definition 3.1. *Given an integer $s \geq 0$ and any $\delta > 0$, if $g^{(1)} \in C^{s+3/2+\delta}$ then, for order–r ($r \in \{0,1\}$) Fourier multipliers $\{Y^{(1)}, Z^{(1)}\}$, if a unique quasiperiodic solution exists of*

$$
\begin{aligned}
&div\left[A^{(0)}\nabla v^{(0)}\right] + k_0^2 v^{(0)} = 0, && a^{(1)} + g^{(1)}(x) < z < \overline{a}, && \text{(14a)}\\
&\partial_z v^{(0)} + T^{(0)}[v^{(0)}] = 0, && z = \overline{a}, && \text{(14b)}\\
&\mathcal{N}^{\ell}(0)[v^{(0)}] - Y^{(1)}[v^{(0)}] = U^{(0),\ell}, && z = a^{(1)} + g^{(1)}(x), && \text{(14c)}
\end{aligned}
$$

we define the upper IIO

$$
Q[U^{(0),\ell}] = Q(\overline{a}, a^{(1)}, g^{(1)})[U^{(0),\ell}] := \tilde{U}^{(0),\ell} = \mathcal{N}^{\ell}(0)[v^{(0)}] + Z^{(1)}[v^{(0)}]. \quad \text{(14d)}
$$

Definition 3.2. *Given an integer $s \geq 0$ and any $\delta > 0$, if $g^{(M)} \in C^{s+3/2+\delta}$ then, for order–r ($r \in \{0,1\}$) Fourier multipliers $\{Y^{(M)}, Z^{(M)}\}$, if a unique quasiperiodic solution exists of*

$$
\begin{aligned}
&div\left[A^{(M)}\nabla v^{(M)}\right] + k_0^2 v^{(M)} = 0, && \underline{a} < z < a^{(M)} + g^{(M)}(x), && \text{(15a)}\\
&\mathcal{N}^{u}(M)[v^{(M)}] - Z^{(M)}[v^{(M)}] = U^{(M),u}, && z = a^{(M)} + g^{(M)}(x), && \text{(15b)}\\
&\partial_z v^{(M)} - T^{(M)}[v^{(M)}] = 0, && z = \underline{a}, && \text{(15c)}
\end{aligned}
$$

we define the lower IIO

$$
S[U^{(M),u}] = S(\underline{a}, a^{(M)}, g^{(M)})[U^{(M),u}] := \tilde{U}^{(M),u} = \mathcal{N}^{u}(M)[v^{(M)}] + Y^{(M)}[v^{(M)}]. \quad \text{(15d)}
$$

Definition 3.3. *Given an integer $s \geq 0$ and any $\delta > 0$, if $g^{(m)}, g^{(m+1)} \in C^{s+3/2+\delta}$ then, for order–r ($r \in \{0,1\}$) Fourier multipliers $\{Y^{(m)}, Y^{(m+1)}, Z^{(m)}, Z^{(m+1)}\}$, if a unique quasiperiodic solution exists of*

$$
\begin{aligned}
&div\left[A^{(m)}\nabla v^{(m)}\right] + k_0^2 v^{(m)} = 0, && a^{(m+1)} + g^{(m+1)}(x) < z < a^{(m)} + g^{(m)}(x), && \text{(16a)}\\
&\mathcal{N}^{u}(m)[v^{(m)}] - Z^{(m)}[v^{(m)}] = U^{(m),u}, && z = a^{(m)} + g^{(m)}(x), && \text{(16b)}\\
&\mathcal{N}^{\ell}(m)[v^{(m)}] - Y^{(m+1)}[v^{(m)}] = U^{(m),\ell}, && z = a^{(m+1)} + g^{(m+1)}(x), && \text{(16c)}
\end{aligned}
$$

we define an inner IIO

$$R^{(m)}\left[\begin{pmatrix} U^{(m),u} \\ U^{(m),\ell} \end{pmatrix}\right] = R^{(m)}(a^{(m)}, g^{(m)}, a^{(m+1)}, g^{(m+1)})\left[\begin{pmatrix} U^{(m),u} \\ U^{(m),\ell} \end{pmatrix}\right]$$
$$= \begin{pmatrix} R^{(m),uu} & R^{(m),u\ell} \\ R^{(m),\ell u} & R^{(m),\ell\ell} \end{pmatrix}\left[\begin{pmatrix} U^{(m),u} \\ U^{(m),\ell} \end{pmatrix}\right]$$
$$:= \begin{pmatrix} \tilde{U}^{(m),u} \\ \tilde{U}^{(m),\ell} \end{pmatrix} = \begin{pmatrix} \mathcal{N}^u(m)[v^{(m)}] + Y^{(m)}[v^{(m)}] \\ \mathcal{N}^\ell(m)[v^{(m)}] + Z^{(m+1)}[v^{(m)}] \end{pmatrix}. \quad (16d)$$

Remark 3.4. *As far as we are aware, the uniqueness of solutions to the problems* (14)*,* (15)*, and* (16) *is still an open question. However, it is known (see, e.g., [50]) that in the case of an isotropic material,* $\epsilon_x^{(m)} = \epsilon_y^{(m)} = \epsilon_z^{(m)}$*, these problems are well–posed provided that*

$$\mathrm{Im}\left\{\int_0^d \left(Y^{(m)}\varphi\right)\bar{\varphi}\,dx\right\} > 0, \quad \mathrm{Im}\left\{\int_0^d \left(Z^{(m)}\varphi\right)\bar{\varphi}\,dx\right\} > 0.$$

Therefore, the choice of Després [42, 43], $Y^{(m)} = Z^{(m)} = i\eta$*,* $\eta > 0$*, ensures well–defined IIOs.*

Following [39] we can write this system of equations as

$$\mathbf{AV} = \mathbf{R}, \quad (17)$$

where

$$\mathbf{V} := \begin{pmatrix} U^{(0),\ell} \\ U^{(1),u} \\ U^{(1),\ell} \\ \vdots \\ U^{(M-1),u} \\ U^{(M-1),\ell} \\ U^{(M),u} \end{pmatrix}, \quad \mathbf{R} := \begin{pmatrix} \zeta^{(1)} \\ \psi^{(1)} \\ \vdots \\ \zeta^{(M)} \\ \psi^{(M)} \end{pmatrix}.$$

Also

$$\mathbf{A} := \begin{pmatrix} \mathbf{D}^{(1)} & \mathbf{U}^{(1)} & 0 & 0 & \cdots & 0 \\ \mathbf{L}^{(2)} & \mathbf{D}^{(2)} & \mathbf{U}^{(2)} & 0 & \cdots & 0 \\ 0 & \ddots & \ddots & \ddots & 0 & 0 \\ 0 & 0 & \ddots & \ddots & \ddots & 0 \\ 0 & \cdots & 0 & \mathbf{L}^{(M-1)} & \mathbf{D}^{(M-1)} & \mathbf{U}^{(M-1)} \\ 0 & \cdots & 0 & 0 & \mathbf{L}^{(M)} & \mathbf{D}^{(M)} \end{pmatrix},$$

where

$$\mathbf{U}^{(m)} = \begin{pmatrix} (I + \tilde{F}^{(m)})R^{(m),u\ell} & 0 \\ \tilde{G}^{(m)}R^{(m),u\ell} & 0 \end{pmatrix}, \quad 1 \le m \le M-1,$$

and

$$\mathbf{L}^{(m)} = \begin{pmatrix} 0 & 0 \\ 0 & R^{(m-1),\ell u} \end{pmatrix}, \quad 2 \le m \le M,$$

and

$$\mathbf{D}^{(1)} = \begin{pmatrix} I & F^{(1)} + (I + \tilde{F}^{(1)})R^{(1),uu} \\ Q & (I + G^{(1)}) + \tilde{G}^{(1)}R^{(1),uu} \end{pmatrix},$$

$$\mathbf{D}^{(m)} = \begin{pmatrix} I & F^{(m)} + (I + \tilde{F}^{(m)})R^{(m),uu} \\ R^{(m-1),\ell\ell} & (I + G^{(m)}) + \tilde{G}^{(m)}R^{(m),uu} \end{pmatrix}, \qquad 2 \le m \le M-1,$$

$$\mathbf{D}^{(M)} = \begin{pmatrix} I & F^{(M)} + (I + \tilde{F}^{(M)})S \\ R^{(M-1),\ell\ell} & (I + G^{(M)}) + \tilde{G}^{(M)}S \end{pmatrix}.$$

4. A High–Order Perturbation of Surfaces Method

At this point we have several options for solving our governing equations, (17). We adopt a geometric perturbation approach based upon the assumption

$$g^{(m)}(x) = \varepsilon f^{(m)}(x), \quad 1 \le m \le M,$$

for ε sufficiently small and $f^{(m)}$ sufficiently smooth (at least $C^{s+3/2+\delta}$ for some $\delta > 0$). In this case, the operator $\mathbf{A} = \mathbf{A}(\varepsilon)$ and the right–hand–side $\mathbf{R} = \mathbf{R}(\varepsilon)$ depend *analytically* upon ε so that

$$\mathbf{A}(\varepsilon) = \sum_{n=0}^{\infty} \mathbf{A}_n \varepsilon^n, \quad \mathbf{R}(\varepsilon) = \sum_{n=0}^{\infty} \mathbf{R}_n \varepsilon^n. \tag{18}$$

With this it can be shown that the solution $V(\varepsilon)$ depends analytically upon ε, so that

$$\mathbf{V}(\varepsilon) = \sum_{n=0}^{\infty} \mathbf{V}_n \varepsilon^n, \tag{19}$$

where, upon insertion of these forms into (17), we find at order $\mathcal{O}(\varepsilon^n)$,

$$\mathbf{A}_0 \mathbf{V}_n = \mathbf{R}_n - \sum_{\ell=0}^{n-1} \mathbf{A}_{n-\ell} \mathbf{V}_\ell,$$

or

$$\mathbf{V}_n = \mathbf{A}_0^{-1}\left[\mathbf{R}_n - \sum_{\ell=0}^{n-1}\mathbf{A}_{n-\ell}\mathbf{V}_\ell\right]. \tag{20}$$

We refer the interested reader to [39] and the references therein for a more formal justification of these developments, in particular, the demonstration that the relevant IIOs, $\{Q, R^{(m)}, S\}$, depend analytically upon the perturbation parameter ε which justifies the expansion of the terms $\{\mathbf{A}, \mathbf{R}\}$ in convergent power series. We further mention that the paper [39] provides a possible path to establishing that, under certain hypotheses, unique solutions of (17) exist.

Remark 4.1. *We anticipate that the smallness assumption on the perturbation variable, ε, can be dropped provided that it is real and that there is no topological obstruction (e.g., intersecting layer interfaces). The papers [51, 52] provide one possible approach to establishing such a result.*

5. Numerical Results

We now present the results of numerical experiments based upon the formulation of grating structures featuring hyperbolic materials stated above. We begin with a brief validation by the Method of Manufactured Solutions and follow up with simulations of structures appearing in the engineering literature.

5.1. Implementation

To simulate layered media problems featuring hyperbolic materials we utilize (17), the surface formulation of the governing equations in terms of IIOs which are functions of the interface height/slope ε,

$$\mathbf{A}(\varepsilon)\mathbf{V}(\varepsilon) = \mathbf{R}(\varepsilon).$$

As in [39], we seek a solution of the form (19) which is truncated after a finite number of orders, $N \geq 0$,

$$\mathbf{V}(\varepsilon) \approx \mathbf{V}^N(\varepsilon) := \sum_{n=0}^{N}\mathbf{V}_n\varepsilon^n. \tag{21}$$

To find the $\mathbf{V}_n$ we must solve (20) for $0 \leq n \leq N$ which, in turn, requires the application of the operators $\mathbf{A}_n$ and the formation of the functions $\mathbf{R}_n$

which come from the series expansions of $\mathbf{A}$ and $\mathbf{R}$, respectively. For this we must be able to evaluate the operators $\{F_n^{(m)}, \tilde{F}_n^{(m)}, G_n^{(m)}, \tilde{G}_n^{(m)}\}$ and the IIOs $\{Q_n, R_n^{(m)}, S_n\}$. For the former, all of the details are provided in the papers [34, 39], while for the latter, the method of Transformed Field Expansions (TFE) [53, 51, 46] was used to simulate the IIOs. Again, all of the relevant details are specified in [34, 39]. To summarize, we used a spectral Fourier–Chebyshev approach [12, 54, 14] where

$$\mathbf{V}_n(x,z) \approx \mathbf{V}_n^{N_x,N_z}(x,z) := \sum_{p=-N_x/2}^{N_x/2-1} \sum_{q=0}^{N_z} \hat{\mathbf{V}}_{n,p,q} T_q(z/h) e^{i\alpha_p x},$$

and T_q is the q–th Chebyshev polynomial. To find the Fourier–Chebyshev coefficients, $\{\hat{\mathbf{V}}_{n,p,q}\}$, we used the collocation method by demanding that the governing equations be true at the gridpoints, e.g. on a layer $\{[0,d]\times[-h,h]\}$,

$$\{x_j = j(d/N_x) \mid 0 \le j \le N_x - 1\}, \quad \{z_r = h\cos(\pi r/N_z) \mid 0 \le r \le N_z\}.$$

With fast Fourier and Chebyshev transforms [12, 54, 14] the resulting equations were solved efficiently and stably.

Remark 5.1. *We point out that these developments eventually lead to the simulation of two–point boundary value problems for the quantities $\hat{\mathbf{V}}_{n,p}(z)$ on $\{-h < z < h\}$ which we successfully addressed with our Chebyshev collocation method. For this, the only (mild) challenge to our algorithm was the indefinite nature of the two–point boundary value problem to be solved. Such difficulties were ameliorated when physically mandated dissipation was considered.*

A final, important, question is how the Taylor series, (21), in ε is summed, e.g., the approximation of $\hat{\mathbf{V}}_{p,q}(\varepsilon)$ by

$$\hat{\mathbf{V}}_{p,q}^N(\varepsilon) := \sum_{n=0}^{N} \hat{\mathbf{V}}_{n,p,q} \varepsilon^n.$$

For this, Padé approximation [55] has been used in conjunction with HOPS methods to great effect [56, 51] and we recommend its use here. Padé approximation seeks to estimate the truncated Taylor series $\hat{\mathbf{V}}_{p,q}^N(\varepsilon)$ by the rational function

$$[L/M](\varepsilon) := \frac{a^L(\varepsilon)}{b^M(\varepsilon)} = \frac{\sum_{\ell=0}^{L} a_\ell \varepsilon^\ell}{1 + \sum_{m=1}^{M} b_m \varepsilon^m}, \quad L + M = N,$$

and

$$[L/M](\varepsilon) = \hat{\mathbf{V}}^N_{p,q}(\varepsilon) + \mathcal{O}(\varepsilon^{L+M+1});$$

well–known formulas for the coefficients $\{a_\ell, b_m\}$ can be found in [55]. This technique has remarkable properties of enhanced convergence, and we refer the interested reader to § 2.2 of Baker & Graves–Morris [55] and the insightful calculations of § 8.3 of Bender & Orszag [57] for a thorough discussion of the capabilities and limitations of Padé approximants.

5.2. Validation

To validate our scheme, we utilized the Method of Manufactured Solutions [58, 59, 60]. To summarize, consider the general system of partial differential equations subject to generic boundary conditions

$$\begin{aligned} \mathcal{P}v &= 0, && \text{in } \Omega, \\ \mathcal{B}v &= 0, && \text{at } \partial\Omega. \end{aligned}$$

It is typically easy to implement a numerical algorithm to solve the nonhomogeneous version of this set of equations

$$\begin{aligned} \mathcal{P}v &= \mathcal{F}, && \text{in } \Omega, \\ \mathcal{B}v &= \mathcal{J}, && \text{at } \partial\Omega. \end{aligned}$$

To test an implementation we began with the "manufactured solution," $\tilde{v}$, and set

$$\mathcal{F}_v := \mathcal{P}\tilde{v}, \quad \mathcal{J}_v := \mathcal{J}\tilde{v}.$$

Thus, given the pair $\{\mathcal{F}_v, \mathcal{J}_v\}$ we had an *exact* solution of the nonhomogeneous problem, namely $\tilde{v}$. While this does not prove an implementation to be correct, if the function $\tilde{v}$ is chosen to imitate the behavior of anticipated solutions (e.g., satisfying the boundary conditions exactly) then this gives us confidence in our algorithm.

For the current implementation we focused upon the three–layer problem ($M = 2$) and considered the quasiperiodic, outgoing solutions of the Helmholtz equation (14a)

$$v^{(0)}_r(x,z) := A^{(0)}_r e^{i\alpha_r x + i\gamma^{(0)}_r z}, \quad r \in \mathbf{Z}, \quad A^{(0)}_r \in \mathbf{C},$$

and their counterparts for (15a)

$$v^{(2)}_r(x,z) := B^{(2)}_r e^{i\alpha_r x - i\gamma^{(2)}_r z}, \quad r \in \mathbf{Z}, \quad B^{(2)}_r \in \mathbf{C}.$$

Further, we considered the quasiperiodic solutions of the Helmholtz equation (16a)

$$v_r^{(1)}(x,z) := A_r^{(1)} e^{i\alpha_r x + i\gamma_r^{(1)} z} + B_r^{(1)} e^{i\alpha_r x - i\gamma_r^{(1)} z}, \quad r \in \mathbf{Z}, \quad A_r^{(1)}, B_r^{(1)} \in \mathbf{C}.$$

We selected two simple sinusoidal profiles

$$g^{(1)}(x) = \varepsilon f^{(1)}(x) = \varepsilon \cos(2x), \quad g^{(2)}(x) = \varepsilon f^{(2)}(x) = \varepsilon \sin(2x), \tag{22}$$

and defined, for any choice of the layer half–thickness $\bar{h}$, the Dirichlet and Neumann traces

$$\begin{aligned}
\xi_r^{(0)}(x) &:= v_r^{(0)}(x, \bar{h} + g^{(1)}(x)), \quad & \nu_r^{(0)}(x) &:= \mathcal{N}^{\ell}(0)[v_r^{(0)}(x, \bar{h} + g^{(1)}(x))], \\
\xi_r^{(1),h}(x) &:= v_r^{(1)}(x, \bar{h} + g^{(1)}(x)), \quad & \nu_r^{(1),h}(x) &:= \mathcal{N}^{u}(1)[v_r^{(1)}(x, \bar{h} + g^{(1)}(x))], \\
\xi_r^{(1),-h}(x) &:= v_r^{(1)}(x, -\bar{h} + g^{(2)}(x)), \quad & \nu_r^{(1),-h}(x) &:= \mathcal{N}^{\ell}(1)[v_r^{(1)}(x, -\bar{h} + g^{(2)}(x))], \\
\xi_r^{(2)}(x) &:= v_r^{(2)}(x, -\bar{h} + g^{(2)}(x)), \quad & \nu_r^{(2)}(x) &:= \mathcal{N}^{u}(2)[v_r^{(2)}(x, -\bar{h} + g^{(2)}(x))].
\end{aligned}$$

From these we defined, for any choices of the operators $\{Y^{(1)}, Z^{(1)}, Y^{(2)}, Z^{(2)}\}$, the impedances

$$V_r^{(0),\ell} := \nu^{(0)} - Y^{(1)}[\xi^{(0)}], \quad \tilde{V}_r^{(0),\ell} := \nu^{(0)} + Z^{(1)}[\xi^{(0)}], \tag{23a}$$

$$V_r^{(1),u} := \nu^{(1),h} - Z^{(1)}[\xi^{(1),h}], \quad \tilde{V}_r^{(1),u} := \nu^{(1),h} + Y^{(1)}[\xi^{(1),h}], \tag{23b}$$

$$V_r^{(1),\ell} := \nu^{(1),-h} - Y^{(2)}[\xi^{(1),-h}], \quad \tilde{V}_r^{(1),\ell} := \nu^{(1),-h} + Z^{(2)}[\xi^{(1),-h}], \tag{23c}$$

$$V_r^{(2),u} := \nu^{(2)} - Z^{(2)}[\xi^{(2)}], \quad \tilde{V}_r^{(2),u} := \nu^{(2)} + Y^{(2)}[\xi^{(2)}]. \tag{23d}$$

We chose the following physical parameters

$$\begin{gathered}
d = 2\pi, \quad \alpha = 0.1, \quad \underline{\underline{\epsilon}}^{(0)} = \underline{\underline{\epsilon}}^{(2)} = \underline{\underline{I}}, \quad \underline{\underline{\epsilon}}^{(1)} = \begin{pmatrix} e + 1.1i & 0 & 0 \\ 0 & e + 1.1i & 0 \\ 0 & 0 & -2.3 + 1.1i \end{pmatrix}, \\
\hat{\sigma}^{(1)} = 0.2, \quad \hat{\sigma}^{(2)} = 0.45, \\
A_r^{(0)} = -3\ \delta_{r,2}, \quad B_r^{(2)} = 4\ \delta_{r,2}, \quad A_r^{(1)} = -e\ \delta_{r,2}, \quad B_r^{(1)} = \pi\ \delta_{r,2},
\end{gathered} \tag{24}$$

(where $\delta_{r,s}$ is the Kronecker delta) in TM polarization, and the numerical parameters

$$N_x = 64, \quad N_z = 24, \quad N = 10, \quad a = 1/5, \quad b = 1/5. \tag{25}$$

To illuminate the behavior of our scheme we made the Després [42, 43, 37] choice of operators

$$Y^{(1)} = Z^{(1)} = Y^{(2)} = Z^{(2)} = i\eta, \quad \eta = k_0, \tag{26}$$

and studied four choices

$$\varepsilon = 0.005, 0.01, 0.05, 0.1,$$

in (22). For this we supplied the "exact" input data, $\{V_r^{(0),\ell}, V_r^{(1),u}, V_r^{(1),\ell}, V_r^{(2),u}\}$, from (23) to our HOPS algorithm to simulate solutions of the IIO formulation of the three–layer scattering problem. We compared the output of this, $\{\tilde{V}_r^{(0),\ell,\text{approx}}, \tilde{V}_r^{(1),u,\text{approx}}, \tilde{V}_r^{(1),\ell,\text{approx}}, \tilde{V}_r^{(2),u,\text{approx}}\}$, with the "exact" output, $\{\tilde{V}_r^{(0),\ell}, \tilde{V}_r^{(1),u}, \tilde{V}_r^{(1),\ell}, \tilde{V}_r^{(2),u}\}$, by computing the relative error

$$\text{Error}_{\text{rel}} := \left|\tilde{V}_r^{(0),\ell} - \tilde{V}_r^{(0),\ell,\text{approx}}\right|_{L^\infty} / \left|\tilde{V}_r^{(0),\ell}\right|_{L^\infty}.$$

We note that the choice to measure the defect in the upper–layer quantity, $\tilde{V}_r^{(0),\ell}$, was arbitrary, and measuring the mismatch in any of the other output quantities produced similar results.

To evaluate our implementation we selected the IIOs specfied by (26), and we report our results in Figures 2 and 3. More specifically, Figure 2 displays both the rapid and stable decay of the relative error as N is increased, and how this rate of decay improves as ε is decreased. Figure 3 shows both how the error shrinks as ε becomes smaller, and that this rate is enhanced as N is increased.

5.3. Comparison with Published Results

Having verified the accuracy and reliability of our implementation we felt justified in simulating results which appear in the engineering literature, in particular the computations published by Kumar *et al* [11]. In this work the authors investigated the dispersion relation of hybrid plasmon–phonon polaritons excited in a configuration consisting of graphene–hBN heterostructures. In this study the tunable graphene surface plasmons which are generated in the mid–infrared to terahertz regime were coupled to the hBN phonon polaritons which also exist in this regime.

Kumar *et al* studied the *linear* dispersion relation for a thin (50 nm thick) layer of hBN in air, and then recomputed this with a monolayer sheet of graphene attached to the hBN. In short, they computed the singularities of

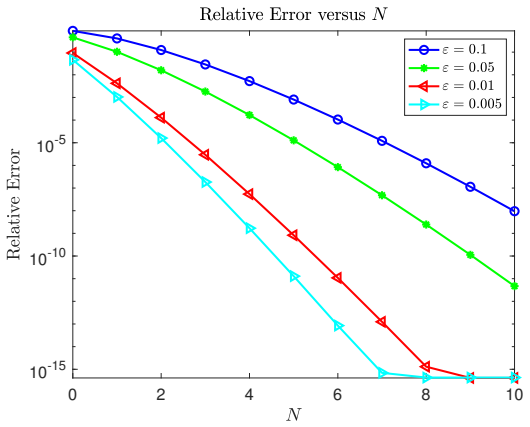

Figure 2: Plot of relative error with six choices of $N = 0, 2, 4, 6, 8, 10$ and four choices of $\varepsilon = 0.005, 0.01, 0.05, 0.1$ for IIO choice (26) with Taylor summation. Physical parameters were (24) and numerical discretization was (25).

$\mathbf{A}_0$, see (18), as the spatial wavenumber $q = 2\pi/d$ and illumination frequency $\omega = 2\pi/\lambda$ were varied. We have reproduced these results in the regimes of Type I hyperbolicity (760 cm^{-1} $< \omega <$ 860 cm^{-1}) without graphene (Figure 4) and with graphene affixed above *and* below the hBN layer (Figure 5). In addition, we have computed in the Type II hyperbolicity range (1000 cm^{-1} $< \omega <$ 1700 cm^{-1}) without graphene (Figure 6) and with graphene above and below the hBN layer (Figure 7).

In these plots we see the characteristic appearance of *multiple* slab polariton modes in the regions of hBN hyperbolicity, $\mathrm{Re}\{\epsilon_x\}\,\mathrm{Re}\{\epsilon_z\} < 0$, indicated by the yellow regions where

$$\log\left(\mathrm{Re}\left\{\Delta\right\}\right) = \log\left(\mathrm{Re}\left\{\mathrm{cond}\mathbf{A}_0\right\}\right), \tag{27}$$

c.f. (18), becomes large, hinting at small values of the dispersion relation. For instance, in Figure 4 we find a range of frequencies between 780 and 830 cm^{-1} which feature *multiple* ranges of large Δ indicating that several modes propagate in the hBN for these frequencies. In addition, we see that the number of such modes increases with increasing ω in Figure 4 (Type I hyperbolicity) and with decreasing ω in Figure 6 (Type II hyperbolicity). Additionally, these figures are *significantly* modified with the introduction of graphene. In both configurations an additional mode, of quite strong magnitude, is introduced at *lower* frequency than the hypebolic regions, which merges rather smoothly to this range as q increases, as noted in [11].

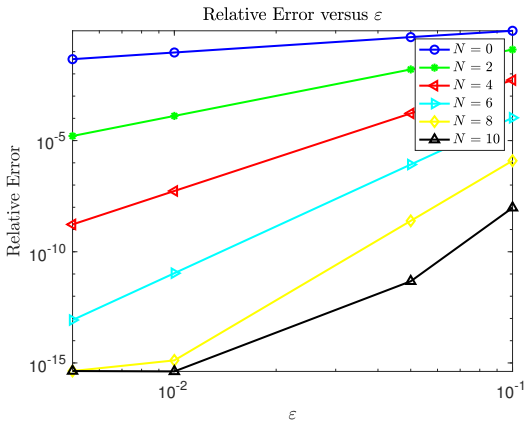

Figure 3: Plot of relative error with six choices of $N = 0, 2, 4, 6, 8, 10$ and four choices of $\varepsilon = 0.005, 0.01, 0.05, 0.1$ for IIO choice (26) with Taylor summation. Physical parameters were (24) and numerical discretization was (25).

Beyond this we can use our solver for (17) to investigate whether one can realize these properties in an actual device. For this we introduce corrugations to the upper air/hBN and lower hBN/air interfaces shaped by

$$f^{(1)}(x) = f^{(2)}(x) = \cos(2\pi x/d),$$

which generate the necessary momentum to realize surface plasmon waves [49]. (We note that, by contrast, Kumar *et al* generate this momentum with periodically spaced *ribbons* of graphene.) We chose the following physical parameters

$$d = 2\pi/q, \quad \theta = 0, \quad \underline{\underline{\epsilon}}^{(0)} = \underline{\underline{\epsilon}}^{(2)} = \underline{\underline{I}}, \quad \underline{\underline{\epsilon}}^{(1)} = \underline{\underline{\epsilon}}^{\mathrm{hBN}}, \quad \hat{\sigma}^{(1)} = \hat{\sigma}^{(2)} = \begin{cases} 0, \\ \hat{\sigma}_D, \end{cases} \tag{28}$$

(see (3) and (8)) in TM polarization, and the numerical parameters

$$N_q = 201, \quad N_\omega = N_q + 1, \quad N_x = 16, \quad N_z = 16, \quad N = 4, \quad a = b = 1/2. \tag{29}$$

Again, we made the Després choice of operators (26) and considered the value $\varepsilon = 0.01$ which is sufficiently large to generate a plasmonic response [61].

To study the response of these configurations under plane–wave illumination we computed the absorbance (the total energy minus the reflected and transmitted energies) which characterizes the energy propagating *inside*

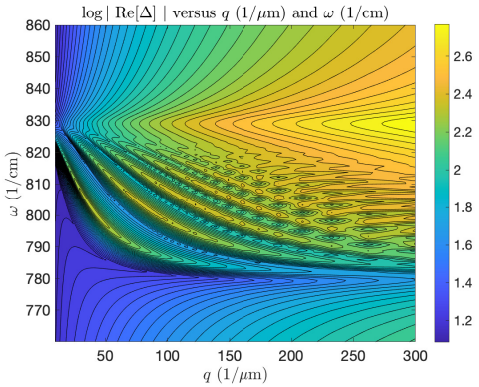

Figure 4: Linear dispersion relation for a layered air/hBN/air structure in the frequency range of Type I hyperbolicity of hBN.

the hBN layer. Here we see in this nonlinear dispersion relation the strong resemblance between our device simulations and the predictions of the linear dispersion relation. More specifically we note the similarities between Figures 4 and 8 in the Type I hyperbolic regime without graphene, Figures 5 and 9 in the Type I hyperbolic regime with graphene, Figures 6 and 10 in the Type II hyperbolic regime without graphene, and Figures 7 and 11 in the Type II hyperbolic regime with graphene. Such results indicate that, in fact, such devices *can* be built and a construction strategy based upon periodically corrugated diffraction gratings is one realistic possibility [62].

Acknowledgments

D.P.N. gratefully acknowledges support from the National Science Foundation through grants No. DMS–1813033 and No. DMS–2111283.

References

[1] J. Pendry, Negative refraction makes a perfect lens, Physical Review Letters 85 (18) (2000) 3966–3969.

[2] D. Smith, J. Pendry, M. Wiltshire, Metamaterials and negative refractive index, Science 305 (2004) 788–792.

[3] B. Wood, J. Pendry, D. Tsai, Directed subwavelength imaging using a layered metal-dielectric system, Physical Review B 74 (2006) 115116.

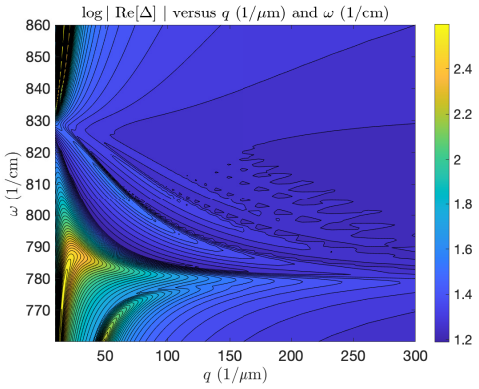

Figure 5: Linear dispersion relation for a layered air/graphene/hBN/graphene/air structure in the frequency range of Type I hyperbolicity of hBN.

[4] A. Poddubny, I. Iorsh, P. Belov, Y. Kivshar, Hyperbolic metamaterials, Nature Photonics 7 (2013) 958–967.

[5] P. Shekhar, J. Atkinson, Z. Jacob, Hyperbolic metamaterials: Fundamentals and applications, Nano Convergence 1 (2014) 17.

[6] L. Ferrari, C. Wu, D. Lepage, X. Zhang, Z. Liu, Hyperbolic metamaterials and their applications, Progress in Quantum Electronics 40 (2015) 1–40.

[7] K. Novoselov, A. Mishchenko, A. Carvalho, A. Castro Neto, 2d materials and van der waals heterostructures, Science 353 (2016) 461.

[8] V. Veselago, The electrodynamics of substances with simultaneously negative values of ϵ and μ, Soviet Physics Uspekhi 10 (4) (1968) 509–514.

[9] D. R. Smith, W. J. Padilla, D. C. Vier, S. C. Nemat-Nasser, S. Schultz, Composite medium with simultaneously negative permeability and permittivity, Phys. Rev. Lett. 84 (2000) 4184–4187.

[10] J. Caldwell, A. Kretinin, Y. Chen, V. Giannini, M. Fogler, Y. Francescato, C. Ellis, J. Tischler, C. Woods, A. Giles, M. Hong, K. Watanabe, T. Taniguchi, S. Maier, K. Novoselov, Sub-diffractional volume-confined polaritons in the natural hyperbolic material hexagonal boron nitride, Nature Communications 5 (1) (2014) 5221.

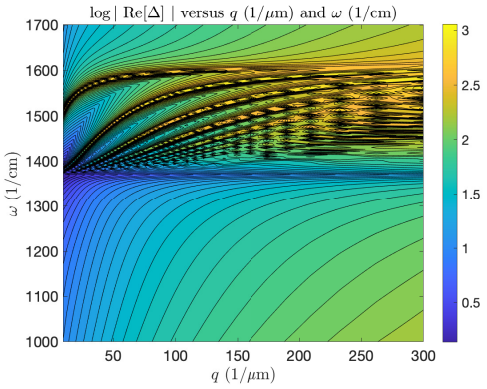

Figure 6: Linear dispersion relation for a layered air/hBN/air structure in the frequency range of Type II hyperbolicity of hBN.

[11] A. Kumar, T. Low, K. Fung, P. Avouris, N. Fang, Tunable light–matter interaction and the role of hyperbolicity in graphene-hbn system, Nano Letters 15 (2015) 3172.

[12] D. Gottlieb, S. A. Orszag, Numerical analysis of spectral methods: theory and applications, Society for Industrial and Applied Mathematics, Philadelphia, Pa., 1977, CBMS-NSF Regional Conference Series in Applied Mathematics, No. 26.

[13] M. O. Deville, P. F. Fischer, E. H. Mund, High-order methods for incompressible fluid flow, Vol. 9 of Cambridge Monographs on Applied and Computational Mathematics, Cambridge University Press, Cambridge, 2002.

[14] J. Shen, T. Tang, L.-L. Wang, Spectral methods, Vol. 41 of Springer Series in Computational Mathematics, Springer, Heidelberg, 2011, algorithms, analysis and applications.

[15] R. J. LeVeque, Finite difference methods for ordinary and partial differential equations, Society for Industrial and Applied Mathematics (SIAM), Philadelphia, PA, 2007, steady-state and time-dependent problems.

[16] C. Johnson, Numerical solution of partial differential equations by the finite element method, Cambridge University Press, Cambridge, 1987.

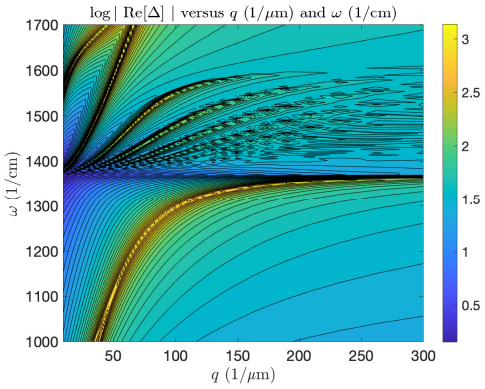

Figure 7: Linear dispersion relation for a layered air/graphene/hBN/graphene/air structure in the frequency range of Type II hyperbolicity of hBN.

[17] J. S. Hesthaven, T. Warburton, Nodal discontinuous Galerkin methods, Vol. 54 of Texts in Applied Mathematics, Springer, New York, 2008, algorithms, analysis, and applications.

[18] COMSOL, COMSOL Multiphysics Reference Manual, COMSOL, Inc., Stockholm, Sweden, 2019.

[19] I.-H. Lee, D. Yoo, P. Avouris, T. Low, S.-H. Oh, Graphene acoustic plasmon resonator for ultrasensitive infrared spectroscopy, Nature Nanotechnology 14 (4) (2019) 313–319.

[20] I.-H. Lee, M. He, X. Zhang, Y. Luo, S. Liu, J. H. Edgar, K. Wang, P. Avouris, T. Low, J. D. Caldwell, S.-H. Oh, Image polaritons in boron nitride for extreme polariton confinement with low losses, Nature Communications 11 (1) (2020) 3649.

[21] D. Colton, R. Kress, Inverse acoustic and electromagnetic scattering theory, 3rd Edition, Vol. 93 of Applied Mathematical Sciences, Springer, New York, 2013.

[22] T. Arens, Scattering by biperiodic layered media: The integral equation approach, Habilitationsschrift, Karlsruhe Institute of Technology (2009).

[23] F. Reitich, K. Tamma, State–of–the–art, trends, and directions in computational electromagnetics, CMES Comput. Model. Eng. Sci. 5 (4) (2004) 287–294.

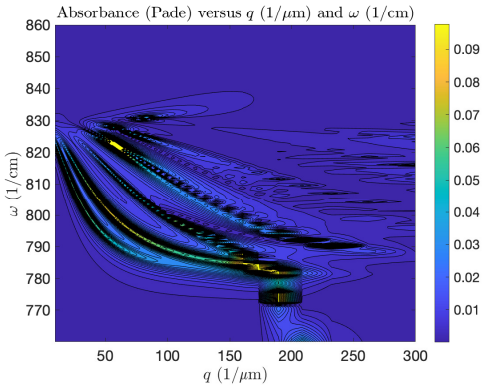

Figure 8: Nonlinear dispersion relation, (27), for a layered air/hBN/air structure in the frequency range of Type I hyperbolicity of hBN.

[24] L. Greengard, V. Rokhlin, A fast algorithm for particle simulations, J. Comput. Phys. 73 (2) (1987) 325–348.

[25] A. Barnett, L. Greengard, A new integral representation for quasi-periodic scattering problems in two dimensions, BIT Numerical Mathematics 51 (2011) 67–90.

[26] O. Bruno, B. Delourme, Rapidly convergent two–dimensional quasi–periodic Green function throughout the spectrum–including Wood anomalies, Journal of Computational Physics 262 (2014) 262–290.

[27] J. Lai, M. Kobayashi, A. Barnett, A fast and robust solver for the scattering from a layered periodic structure containing multi-particle inclusions, J. Comput. Phys. 298 (2015) 194–208.

[28] M. H. Cho, A. Barnett, Robust fast direct integral equation solver for quasi–periodic scattering problems with a large number of layers, Optics Express 23 (2) (2015) 1775–1799.

[29] O. P. Bruno, M. Lyon, C. Pérez-Arancibia, C. Turc, Windowed Green function method for layered-media scattering, SIAM J. Appl. Math. 76 (5) (2016) 1871–1898.

[30] O. P. Bruno, S. P. Shipman, C. Turc, S. Venakides, Superalgebraically convergent smoothly windowed lattice sums for doubly peri-

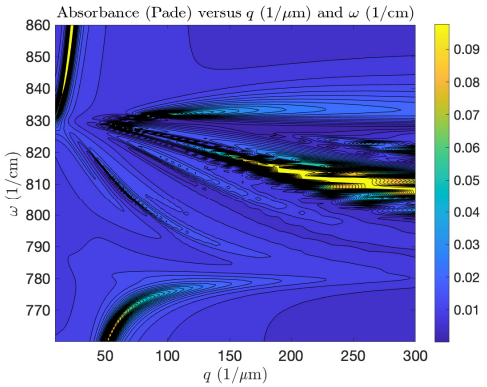

Figure 9: Nonlinear dispersion relation, (27), for a layered air/graphene/hBN/graphene/air structure in the frequency range of Type I hyperbolicity of hBN.

odic Green functions in three-dimensional space, Proc. A. 472 (2191) (2016) 20160255, 19.

[31] O. P. Bruno, A. G. Fernandez-Lado, Rapidly convergent quasi-periodic Green functions for scattering by arrays of cylinders—including Wood anomalies, Proc. A. 473 (2199) (2017) 20160802, 23.

[32] O. P. Bruno, C. Pérez-Arancibia, Windowed Green function method for the Helmholtz equation in the presence of multiply layered media, Proc. A. 473 (2202) (2017) 20170161, 20.

[33] D. P. Nicholls, A method of field expansions for vector electromagnetic scattering by layered periodic crossed gratings, Journal of the Optical Society of America, A 32 (5) (2015) 701–709.

[34] D. P. Nicholls, Stable, high–order computation of impedance–impedance operators for three–dimensional layered media simulations, Proc. Roy. Soc. Lond., A 474 (2018) 20170704.

[35] Y. Hong, D. P. Nicholls, A high–order perturbation of surfaces method for vector electromagnetic scattering by doubly layered periodic crossed gratings, J. Comput. Phys. 372 (2018) 748–772.

[36] D. P. Nicholls, X. Tong, Simulation of localized surface plasmon reso-

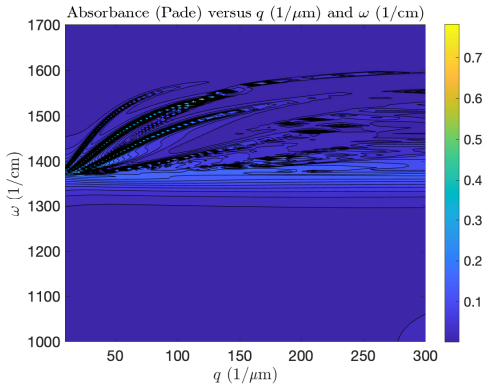

Figure 10: Nonlinear dispersion relation, (27), for a layered air/hBN/air structure in the frequency range of Type II hyperbolicity of hBN.

nances in two dimensions via impedance–impedance operators, SIAM Journal on Applied Mathematics 81 (3) (2021) 871–896.

[37] F. Collino, S. Ghanemi, P. Joly, Domain decomposition method for harmonic wave propagation: a general presentation, Comput. Methods Appl. Mech. Engrg. 184 (2-4) (2000) 171–211, vistas in domain decomposition and parallel processing in computational mechanics.

[38] A. Gillman, A. Barnett, P. Martinsson, A spectrally accurate direct solution technique for frequency-domain scattering problems with variable media, BIT Numer. Math. 55 (1) (2015) 141–170.

[39] D. P. Nicholls, On analyticity of scattered fields in layered structures with interfacial graphene, Studies in Applied Mathematics 147 (2021) 527–576.

[40] D. P. Nicholls, On analyticity of linear waves scattered by a layered medium, Journal of Differential Equations 263 (8) (2017) 5042–5089.

[41] P.-L. Lions, On the Schwarz alternating method. III. A variant for nonoverlapping subdomains, in: Third International Symposium on Domain Decomposition Methods for Partial Differential Equations (Houston, TX, 1989), SIAM, Philadelphia, PA, 1990, pp. 202–223.

[42] B. Després, Méthodes de décomposition de domaine pour les problèmes de propagation d'ondes en régime harmonique. Le théorème de Borg

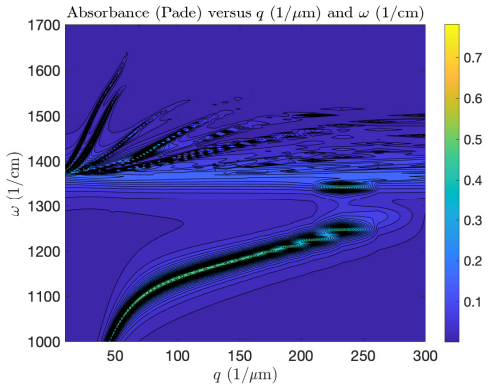

Figure 11: Nonlinear dispersion relation, (27), for a layered air/graphene/hBN/graphene/air structure in the frequency range of Type II hyperbolicity of hBN.

pour l'équation de Hill vectorielle, Institut National de Recherche en Informatique et en Automatique (INRIA), Rocquencourt, 1991, thèse, Université de Paris IX (Dauphine), Paris, 1991.

[43] B. Després, Domain decomposition method and the Helmholtz problem, in: Mathematical and numerical aspects of wave propagation phenomena (Strasbourg, 1991), SIAM, Philadelphia, PA, 1991, pp. 44–52.

[44] J. Lin, An adaptive boundary element method for the transmission problem with hyperbolic metamaterials, submitted (2021) 25.

[45] J. D. Jackson, Classical electrodynamics, 2nd Edition, John Wiley & Sons Inc., New York, 1975.

[46] D. P. Nicholls, F. Reitich, Shape deformations in rough surface scattering: Improved algorithms, J. Opt. Soc. Am. A 21 (4) (2004) 606–621.

[47] D. P. Nicholls, Numerical simulation of grating structures incorporating two–dimensional materials: A high–order perturbation of surfaces framework, SIAM Journal on Applied Mathematics 78 (1) (2018) 19–44.

[48] Y. Bludov, A. Ferreira, N. Peres, M. Vasilevskiy, A primer on surface plasmon–polaritons in graphene, International Journal of Modern Physics B 27 (2013) 1341001.

[49] P. A. D. Goncalves, N. M. R. Peres, An Introduction to Graphene Plasmonics, World Scientific, Singapore, 2016.

[50] D. P. Nicholls, C. Pérez-Arancibia, C. Turc, Sweeping Preconditioners for the Iterative Solution of Quasiperiodic Helmholtz Transmission Problems in Layered Media, J. Sci. Comput. 82 (2) (2020) 44.

[51] D. P. Nicholls, F. Reitich, Analytic continuation of Dirichlet-Neumann operators, Numer. Math. 94 (1) (2003) 107–146.

[52] D. P. Nicholls, M. Taber, Joint analyticity and analytic continuation for Dirichlet–Neumann operators on doubly perturbed domains, J. Math. Fluid Mech. 10 (2) (2008) 238–271.

[53] D. P. Nicholls, F. Reitich, A new approach to analyticity of Dirichlet-Neumann operators, Proc. Roy. Soc. Edinburgh Sect. A 131 (6) (2001) 1411–1433.

[54] J. Shen, T. Tang, Spectral and high-order methods with applications, Vol. 3 of Mathematics Monograph Series, Science Press Beijing, Beijing, 2006.

[55] G. A. Baker, Jr., P. Graves-Morris, Padé approximants, 2nd Edition, Cambridge University Press, Cambridge, 1996.

[56] O. Bruno, F. Reitich, Numerical solution of diffraction problems: A method of variation of boundaries. II. Finitely conducting gratings, Padé approximants, and singularities, J. Opt. Soc. Am. A 10 (11) (1993) 2307–2316.

[57] C. M. Bender, S. A. Orszag, Advanced mathematical methods for scientists and engineers, McGraw-Hill Book Co., New York, 1978, international Series in Pure and Applied Mathematics.

[58] O. R. Burggraf, Analytical and numerical studies of the structure of steady separated flows, J. Fluid Mech. 24 (1966) 113–151.

[59] P. J. Roache, Code verification by the method of manufactured solutions, J. Fluids Eng. 124 (1) (2002) 4–10.

[60] C. J. Roy, Review of code and solution verification procedures for computational simulation, J. Comp. Phys. 205 (1) (2005) 131–156.

[61] D. P. Nicholls, S.-H. Oh, Launching graphene surface plasmon waves with vanishingly small periodic grating structures, Journal of the Optical Society of America, A 38 (4) (2021) 556–563.

[62] N. Lassaline, R. Brechbühler, S. Vonk, K. Ridderbeek, M. Spieser, S. Bisig, B. le Feber, F. Rabouw, D. Norris, Optical fourier surfaces, Nature 582 (2020) 506–510.